



## A sustainable $\delta$ -MnO<sub>2</sub> derived from Amazon rainforest Mn-ore tailings for applications in lithium-ion batteries

L. Angeletti<sup>a,1</sup>, M. Agostini<sup>b,\*</sup>, B.A. Miranda Figueira<sup>c</sup>, A. Latini<sup>a</sup>, E.C. Paris<sup>d</sup>, F. De Giorgio<sup>e</sup>, T. Schultz<sup>f</sup>, C. Di Conzo<sup>g</sup>, F. Mura<sup>h,i</sup>, M. Rossi<sup>h,i</sup>, N.G. Yadav<sup>j</sup>, P. Adelhelm<sup>f,j</sup>, F. Mazzei<sup>b</sup>, S. Brutti<sup>a</sup>, S. Quaranta<sup>k,\*</sup>

<sup>a</sup> Department of Chemistry, Sapienza University of Rome, P.le Aldo Moro 5, 00185 Rome, Italy

<sup>b</sup> Department of Chemistry and Drug Technologies, Sapienza University of Rome, P.le Aldo Moro 5, 00185 Rome, Italy

<sup>c</sup> Post-graduate Program of Science and Engineering of Materials, Federal University of Pará, Conjunto Cidade Nova 4, Travessa WE Vinte e Seis, 2 - Bairro Coqueiro – CEP, 67130-660 Ananindeua, Pará, Brazil

<sup>d</sup> Nanotechnology National Laboratory for Agriculture (LNNA), Embrapa Instrumentação, São Carlos 13560-970, Brazil

<sup>e</sup> Institute of Nanostructured Materials, Italian National Research Council (ISMN-CNR), Via Piero Gobetti, 101, 40141 Bologna, Italy

<sup>f</sup> Helmholtz Zentrum Berlin, Hahn-Meitner-Platz 1, 14109 Berlin, Germany

<sup>g</sup> Department of Applied Science and Technology (DISAT), Polytechnic of Turin, Corso Castelfidardo 39, Turin, Italy

<sup>h</sup> Department of Basic and Applied Science for Engineering, Sapienza University of Rome, Via Scarpa 14, 00161 Rome, Italy

<sup>i</sup> Research Center on Nanotechnologies Applied to Engineering of Sapienza (CNIS), Sapienza University of Rome, P.le Aldo Moro 5, 00185 Rome, Italy.

<sup>j</sup> Department of Chemistry, Humboldt University, 2.304, Brook-Taylor-Str. 2, Adlershof, 12489 Berlin, Germany

<sup>k</sup> Institute for the Study of Nanostructured Materials, Italian National Research Council (ISMN-CNR), Strada Provinciale 35d 9, 00010 Rome, Italy

### ARTICLE INFO

#### Keywords:

Green recovery  
 $\delta$ -MnO<sub>2</sub> electrodes  
 Lithium-ion batteries (LIBs)  
 Manganese-based tailings  
 Rechargeable lithium batteries

### ABSTRACT

The transition to net-zero emissions by 2050 necessitates the development of sustainable and efficient energy storage systems to complement the rise in renewable energy generation. Lithium-ion batteries (LiBs) are pivotal in this energy transformation, yet challenges remain in developing sustainable, high-performance materials. Manganese oxides (MnO<sub>x</sub>) are promising candidates for LiBs anodes due to their abundance and high theoretical capacity. However, the commercial synthesis of MnO<sub>x</sub> materials is resource-intensive, and the mining processes generate large amounts of environmentally hazardous tailings. In this study, we propose a novel method to recover manganese from mining tailings in the Brazilian Amazon and synthesize  $\delta$ -MnO<sub>2</sub> as a high-capacity conversion anode material for LIBs. Using a green recovery method involving KOH and H<sub>2</sub>O<sub>2</sub>, we extracted potassium manganate (K<sub>2</sub>MnO<sub>4</sub>) from the tailings with a recovery efficiency of 90.3 %, and synthesized  $\delta$ -MnO<sub>2</sub>. The prepared material showed promising electrochemical properties, demonstrating its potential as a sustainable alternative to commercially available manganese oxides. This process not only offers a way to mitigate the environmental risks posed by manganese mining tailings but also provides an economically viable solution for producing high-performance battery materials. The developed methodology can be applied to other manganese-bearing residues and low-grade ores, contributing to the growing demand for battery-grade manganese in a sustainable and circular manner.

### 1. Introduction

Achieving net-zero emissions by 2050 requires the immediate and massive deployment of clean and efficient energy technologies. Therefore, renewable energy sources, such as solar and wind, will play a critical role in this transition, with their share in total electric power

generation expected to increase from 29 % in 2020 to over 60 % by 2030 and nearly 90 % by 2050 (IEA 2021). However, renewable energies are inherently intermittent, highlighting the need for reliable and sustainable energy storage systems to ensure a continuous and stable electricity supply [1]. Among energy storage technologies, lithium-ion batteries (LiBs) are currently the leading solution due to their high energy density

\* Corresponding authors.

E-mail addresses: [marco.agostini@uniroma1.it](mailto:marco.agostini@uniroma1.it) (M. Agostini), [simone.quaranta@cnr.it](mailto:simone.quaranta@cnr.it) (S. Quaranta).

<sup>1</sup> equally contributed

and efficiency [2]. Currently commercial LiBs rely on cathode featuring non-abundant elements such as Ni and Co, while the anode is based on graphite. However, challenges developing sustainable and scalable materials for future LiBs still remain [3]. The replacement of graphite is a key area of research, driven by the need for higher energy density, faster charging, and improved battery lifespan. While graphite electrodes offer reliability, their limitations in energy storage systems have prompted scientists to explore alternative materials, in particular those based on conversion chemistries [4]. Manganese oxides ( $MnO_x$ ) have been emerging as promising materials for LiBs anodes owing to their natural abundance, good chemical stability, and high theoretical capacity [5,6].  $MnO_x$ -based anodes, which include a variety of different oxidation state oxides ( $MnO$ ,  $MnO_2$ ,  $Mn_2O_3$ ,  $Mn_3O_4$ ), are particularly attractive because of their potential to store large amounts of lithium. Despite these advantages,  $MnO_x$ -based anodes face several limitations, such as low electrical conductivity, poor ion diffusion, and structural degradation during charge and discharge cycles, leading to capacity fading [7,8].

Currently, around 90 % of extracted manganese is used in the steel industry, and manganese oxides for batteries are predominantly synthesized from commercially available chemicals. Thus, manganese sources are a great challenge in the development of  $MnO_x$ -based electrodes. In fact, the extraction and processing of high-grade manganese ores, are resource-intensive and lead to significant environmental impact [9]. Besides, the mining and beneficiation processes generate substantial amounts of manganese tailings, which are stockpiled in dams or illegally traded. These tailings pose environmental and social risks, particularly in countries like Brazil [10]. Considering the rapidly growing demand for manganese sources, the European Union has classified battery-grade manganese as a critical raw material (CRM). The EU Critical Raw Materials Act (2024) requires member states to ensure that 10 % of their manganese supply comes from domestic sources and that

25 % of this supply is recovered from secondary sources such as industrial waste [11]. This stresses the importance of finding more sustainable and economically viable sources of manganese for battery production. In this respect, Mn-ore mining tailings are particularly intriguing as secondary raw material since are comprised of relatively large amounts of manganese-bearing minerals that are regarded as non-suitable for the steel industry [12]. This paper proposes a novel approach to recover manganese from mining tailings in the Brazilian Amazon Rainforest, i.e. from the Kalunga Dam (Pará), and to synthesize a high-capacity conversion anode material for lithium-ion batteries. Specifically, we developed a non-stoichiometric  $\delta$ - $MnO_2$  material with potential applications in lithium metal batteries by means of a sustainable method which can offer a way to mitigate environmental risks while contributing to the growing demand for battery-grade manganese.

## 2. Results and discussion

### 2.1. Recovery of $MnO_x$ from mining tailings

Fig. 1 presents the chemical and mineralogical characteristics of Mn-tailings. In particular, the tailings consist of approximately 16 % manganese by weight, along with notable amounts of aluminum (9.8 %), silicon (8.8 %), and iron (5.6 %). The mineralogical composition is influenced by the original ore formation—mainly pyrolusite and cryptomelane—and by the various beneficiation processes employed, including washing, jigging, crushing, clay scrubbing, grinding, sieving with vibrating screens, hydraulic classification, and sink-and-float separation. As a consequence, the tailings also contain “light” (specific gravity  $\approx 3$ –3.8) and “soft” (Mohs hardness  $\approx 1.5$ ) manganese oxides with layered (birnessite) or tunneled (todorokite) structures, which accumulated alongside low-density minerals like quartz, kaolinite, and gibbsite. XRF elemental analysis detected Ba, Ca, and K, which originate

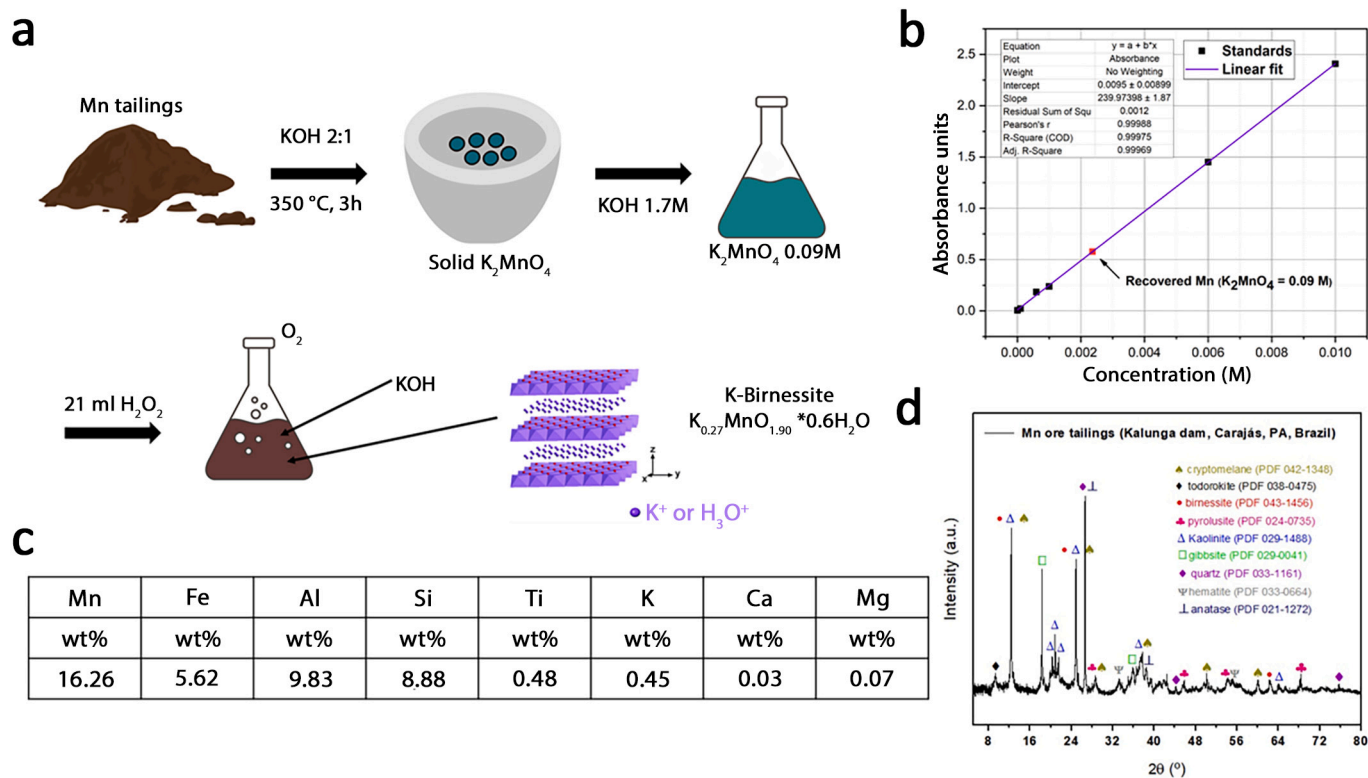


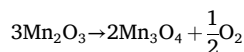
Fig. 1. Schematic of  $K_2MnO_4$  recovery and  $MnO_x$  synthesis from mining tailings. The synthetic pathway of  $MnO_x$  recovery via alkaline fusion and  $H_2O_2$  reduction is illustrated here. Starting from tailings, the Mn is recovered as a  $K_2MnO_4$  solution and finally transformed into  $\delta$ - $MnO_2$  (M1). a) Mn recovery and M1 synthesis; b) calibration curve to evaluate spectrophotometrically Mn extraction efficiency (through the  $\lambda = 525\text{ nm}$   $KMnO_4$  absorption peak); c) elemental tailings composition and d) X-ray diffraction pattern of recovered  $\delta$ - $MnO_2$ .

from non-stoichiometric manganese oxides such as cryptomelane, birnessite, and todorokite. Thermal analysis of the tailings revealed “low temperature” endothermic losses primarily associated with gibbsite dehydroxylation in two steps (at 264 and 354 °C), see Fig. S1 in Supporting Information. These losses overlap with the progressive water loss from Mn-bearing birnessite and todorokite, transforming into cryptomelane, as well as kaolinite dehydration to metakaolinite [13–15]. Additionally, incomplete transformation of manganese phases into Mn<sub>2</sub>O<sub>3</sub> is observed at around 600 °C, while the conversion of cryptomelane to Mn<sub>2</sub>O<sub>3</sub> occurs between 650 and 780 °C. The complete transformation of manganese ore tailings into Mn<sub>3</sub>O<sub>4</sub> (bixbyite-to-hausmannite transition) is achieved at 985 °C, accompanied by the loss of half a mole of oxygen. As for Mn recovery process, manganese leaching rate, measured as K<sub>2</sub>MnO<sub>4</sub> extraction efficiency, see Fig. 1, reached 90.3 %. Although this extraction yield is high, efforts are underway to optimize the process in terms of the cost-benefit ratio, particularly the KOH-to-tailings ratio. The current methodology is to be considered suitable to be applied not only to the present tailings but also to various types of manganese-bearing mining residues, including silicates, as well as to low-grade manganese ores not intended for steel production [16,17]. Overall, the current methodology is highly versatile and can be applied to various types of manganese ores and extraction residues, regardless of their chemical composition, including braunite, rhodochrosite, and manganese silicates. Nonetheless, the manganese recovery process becomes more and more advantageous when it comes to ores with low silica and low alumina content. Therefore, the alkaline fusion process is expected to be particularly profitable when applied to ores or tailings with low aluminum and silicon content, such as those found in decommissioned mines across the Northern Brazilian Amazon [14,15].

## 2.2. Physical-chemical characterization of $\delta$ -MnO<sub>2</sub> powder

After recovery, potassium manganate was converted into the M1 material using H<sub>2</sub>O<sub>2</sub>, and its physicochemical properties were investigated. Manganese average oxidation state (AOS) in the M1 powder, determined by the oxalate back-titration method, was found to be 3.53 ± 0.05. Combination of flame atomic absorption spectroscopy (FAAS) results (K = 8.1 wt%, Mn = 41.7 wt%), AOS determination, and thermal analysis, see Fig. S2 in SI section, led to an M1 composition corresponding to K<sub>0.27</sub>MnO<sub>1.90</sub>·0.6H<sub>2</sub>O (commonly reported as K<sub>0.27</sub>MnO<sub>2</sub>·0.6H<sub>2</sub>O). The presence of oxygen vacancies and structural water is expected to significantly influence the electrochemical properties of the material. The composition of M1 aligns with manganese oxides prepared through potassium permanganate reduction. Additionally, FAAS analysis showed that residual levels of iron (0.008 %) and aluminum (0.076 %) in M1 are negligible and can be safely disregarded. M1 thermal analysis is reported in Fig. S2, SI section. The lowest temperature thermal event corresponds to the elimination of physisorbed H<sub>2</sub>O. Surface water evaporation is accomplished at 101 °C. Further mass loss, with a maximum slope at 145 °C, can be associated with the elimination of interlayer (i.e. crystallization) water [18–20]. The observed weight loss between 120 °C and 500 °C was 8.7 %, and can be ascribed to the removal of residual crystallization water and surface OH groups. Such dehydration facilitates the phase transition from  $\delta$ -MnO<sub>2</sub> (layered) to  $\alpha$ -MnO<sub>2</sub> (tunneled). Indeed, birnessite-like materials with a K/Mn ratio between 0.1 and 0.3 are known to exothermically crystallize into tunneled cryptomelane (KMn<sub>8</sub>O<sub>16</sub>). The closer the K/Mn ratio to 0.125, the sharper the differential thermal analysis (DTA) exothermic peak associated with the birnessite-to-cryptomelane transition [21]. Since the K/Mn ratio for M1 is 0.27, deviating significantly from 0.125, the corresponding DTA exothermic signal is broad. Upon further heating, M1 decomposes into K<sub>2</sub>Mn<sub>4</sub>O<sub>4</sub> and bixbyite (Mn<sub>2</sub>O<sub>3</sub>). The decomposition of MnO<sub>2</sub> to Mn<sub>2</sub>O<sub>3</sub>, with the release of oxygen, occurs at about 580 °C, as indicated by a downward peak in the DTA signal. Finally, the conversion

of manganese sesquioxide to Mn<sub>3</sub>O<sub>4</sub> occurs above 900 °C, according to the following reaction:



Consequently, M1 exhibited a sharp endothermic peak and a significant mass loss between 900 °C and 1100 °C, amounting to about 3.7 wt%. This loss corresponds to the release of half a molecule of O<sub>2</sub>, confirming the transition to the mixed-valence (II/III) manganese oxide.

Fig. 2 provides a comprehensive morphological and structural analysis of the M1 material. In Fig. 2a, scanning electron microscopy (SEM) images and energy-dispersive X-ray spectroscopy (EDS) maps illustrate the salient sample features. The morphology of M1 consists of nanometric “sheets” organized into a hierarchical, flower-like, “spongy” structure. These nanometric particles developed into submicron-sized formations (300–400 nm), resulting in a macroporous structure with pore sizes around 70 nm. This type of morphology is characteristic of non-stoichiometric manganese oxides synthesized by reducing KMnO<sub>4</sub>, particularly using ethanol or hydrogen peroxide [22–25]. The EDS maps further demonstrate the uniform composition of M1. Indeed, the EDS spectrum shows no detectable iron or aluminum and only a minimal silicon signal, reinforcing the FAAS findings regarding the purity of the material. It has to be taken into account that the carbon signals from EDS analysis is originated from the carbon tape. To gain deeper insights into the morphology of M1 and its implications for electrode performance, SEM analyses were also conducted on M1-based conversion anodes before cycling, Fig. S3 in the SI section. The hierarchical, flower-like structure of M1 particles was preserved in the electrodes, and the material’s purity was maintained. For comparison, SEM analyses of electrodes prepared using M2–M5 materials are also presented in Fig. S3, SI section. Notably, M2 electrodes exhibited a similar porous, hierarchical structure due to oxygen evolution during the synthesis. In contrast, M3 (produced via manganate disproportionation) displayed a completely disordered morphology with large manganese oxide aggregates. Similar disordered structures were observed for M4 and M5. High-resolution transmission electron microscopy (HR-TEM) analysis of M1, Fig. 1a, reveals agglomerated microporous structures and nanosheet-like building blocks, which contribute to the macroporous structure seen in the SEM images [25–27]. Furthermore, M1 was revealed to be nanocrystalline with plenty of randomly-oriented crystallites as confirmed by Rietveld analysis which revealed an average crystallite size of approximately 7.5 nm. EDS mapping reported in Fig. S4 SI section, identified potassium, manganese, and oxygen, corresponding to manganese oxide, while minor tungsten and silicon contamination, most likely coming from sample handling, was also detected. For sake of comparison, EDS analysis on M2 sample showed no residual contaminants (Al, Fe, Si), while other samples showed significant amounts of Al and Si. This is due to different reduction conditions, see Table S1, that brought about the hydrolysis and precipitation of alkali-soluble species, present in the recovered K<sub>2</sub>MnO<sub>4</sub> solution. Thus, the decrease of pH caused aluminate (most likely KAlO<sub>2</sub>) and potassium silicate (K<sub>3</sub>SiO<sub>3</sub>) precipitation as Al(OH)<sub>3</sub> and amorphous hydrated silica, respectively. Conversely, M4 and M5 are mostly not affected by Al and Si contamination, being synthesized through the reduction of permanganate and manganate, respectively. Still, very small amounts of Al and Si were found together with fluorine that can be attributed to the PVDF binder. This implies that, among the different synthetic routes, K<sub>2</sub>MnO<sub>4</sub> reduction by H<sub>2</sub>O<sub>2</sub> pre-empts Al and Si contamination of the final  $\delta$ -MnO<sub>2</sub> material. Reasonably, convective motion set by oxygen bubbling keeps aluminates and silicates from depositing on the M1 and M2 oxides.

Average crystalline plane distances were inferred from Selected Area Electron Diffraction (SAED) pattern, where five diffraction rings were assigned to the (001), (002), (11 $\bar{1}$ ), (112), and (31 $\bar{2}$ ) crystallographic planes of K-birnessite, Fig. S4 SI section. The X-ray diffraction (XRD) pattern of Fig. 2b further confirms the nanocrystalline nature of M1, showing broad peaks consistent with  $\delta$ -MnO<sub>2</sub> phase (PDF card No.

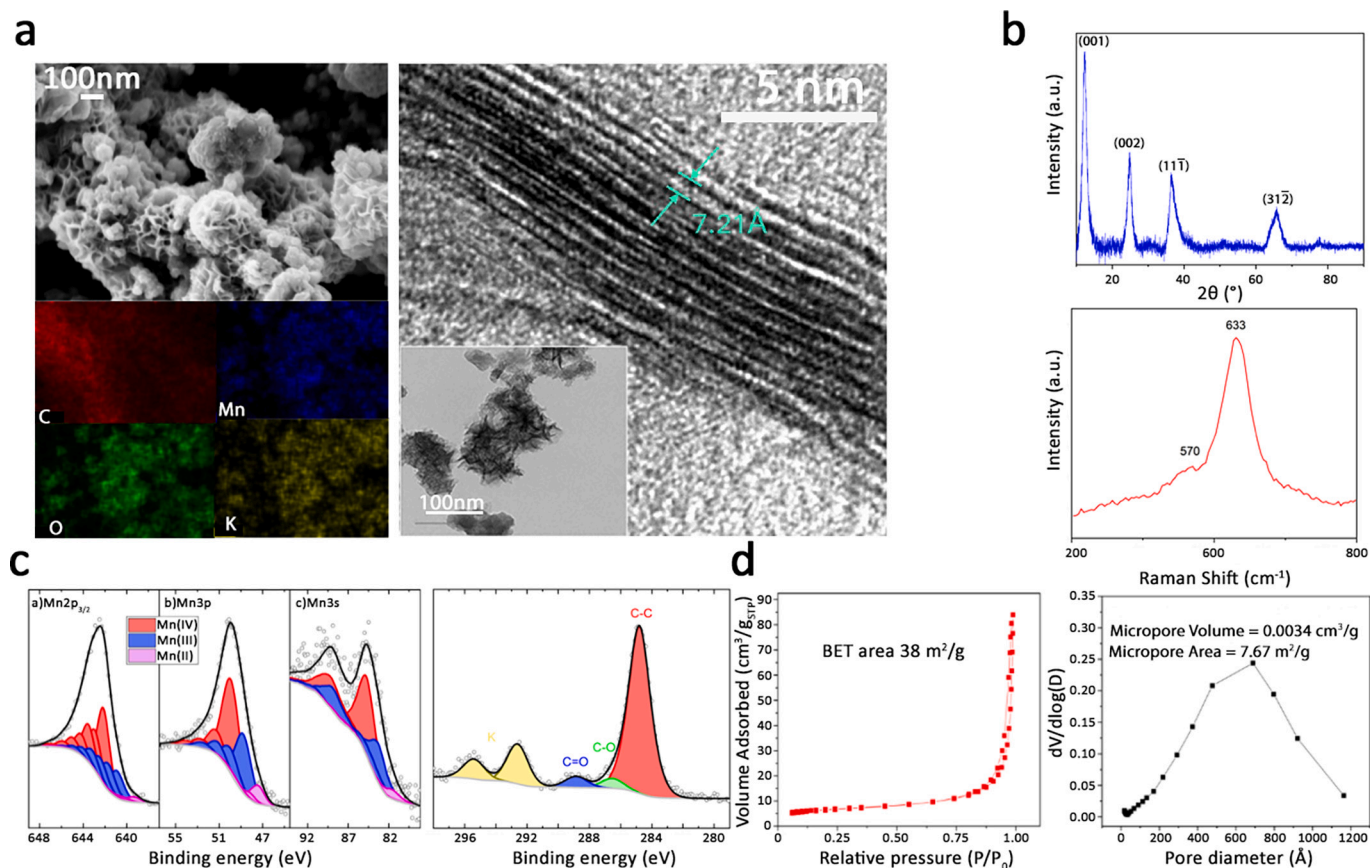


**Fig. 2.** Physical-chemical characterization of material M1. (a) Scanning electron microscopy image (SEM), corresponding EDS mapping of C, Mn, O, K and High Resolution Transmission Electron Microscopy ((001) planes with typical birnessite d-spacing ( $\approx 7 \text{ \AA}$ )). (b) X-ray diffraction pattern (top-panel) and Raman spectrum (down panel). (c) X-ray photoelectron spectroscopy spectra of Mn $2p_{3/2}$ , Mn $3p$ , Mn $3s$  and C $1s$  core level. (d) Nitrogen adsorption-desorption isotherms and the corresponding pore size distribution.

42–1317). The reduction of  $K_2MnO_4$  with  $H_2O_2$  resulted in the formation of this nanocrystalline  $\delta$ - $MnO_2$ , which is in line with previous studies [28–30]. The synthesized material is verified to be a non-stoichiometric, hydrated manganese oxide with a “birnessite-like” hexagonal structure, as evidenced by the diffraction peaks at,  $2\theta \approx 36.5^\circ$  ( $11\bar{1}$  reflection), and  $2\theta \approx 66.0^\circ$  ( $31\bar{2}$  reflection) [25,31]. These diffraction intensities depend on the crystalline degree and grain size [32]. Additionally, the typical layered arrangement of birnessite, with the diffraction peak at  $2\theta = 12.26^\circ$  (001) corresponding to an interlayer spacing of  $7.21 \text{ \AA}$ , was observed, see Fig. 2a. This involves the intercalation of potassium (K) and water ( $H_2O$ ) molecules between  $MnO_6$  octahedral layers. The (002) plane, identified at  $2\theta = 24.85^\circ$  and corresponding to a d-spacing of  $3.58 \text{ \AA}$ , further supports these findings about M1 structure. The XRD pattern shows peak broadening, which is likely due to the nanostructured nature of the material, comprising nanosheets aggregated into nanoparticles. The rapid reaction rate, driven by the addition of hydrogen peroxide to the alkaline manganate solution, probably caused the formation of numerous small crystallization nuclei that did not have time to develop into larger crystals. Thus, the growth of large crystallites was hindered, which explains the broad diffraction peaks observed in Fig. 2b, corroborates the nanocrystalline nature of the material. Nevertheless, the (001) and (002) birnessite basal plane reflections in M1 are more intense than the ( $11\bar{1}$ ) reflection, indicating a certain level of structural order, particularly a consistent interlayer spacing [33]. For comparison, the XRD spectra of M2–M5 materials were also analyzed, as reported in Fig. S5 SI section. Although M2 was synthesized similarly to M1 (by reducing a  $0.05 \text{ M } K_2MnO_4$  solution with  $12 \text{ mL of } H_2O_2$ ) its XRD pattern display a weaker (001) reflection and a more intense ( $11\bar{1}$ ) peak

compared to the (002) reflection. This implies a non-uniform distribution of the interlayer species, in spite of a constant spacing between the  $MnO_6$  octahedral layers [33]. The diffraction pattern of M5, prepared by reducing  $K_2MnO_4$  with absolute ethanol, shows similar features. The disordered distribution of interlayer species in M5, combined with a potential shift of the main Mn–O layers within their planes, results in a less intense and broader (001) reflection compared to M1 [34]. In contrast, samples M3 and M4 exhibited the highest degree of disorder. Their XRD patterns show only the ( $11\bar{1}$ ) and ( $31\bar{2}$ ) peaks, reflecting variable distances between Mn–O layers and a lack of constant interlayer spacing. This irregular spacing, along with the uneven distribution of potassium ions and water molecules, caused turbostratic disorder. Besides, the diffraction peaks of M3 and M4 are extremely broad due to the very small crystallite size, which further verifies the higher disorder compared to the relatively more crystalline M1, M2, and M5 materials. The Raman spectrum reported in Fig. 2b confirms the identification of M1 as birnessite, with a distinct peak at  $633 \text{ cm}^{-1}$  that can be attributed to the  $A_{1g}$  symmetric stretching vibration  $\nu_2(Mn-O)\nu_2(Mn-O)$  of the  $[MnO_6]$  octahedra in triclinic birnessite. Additionally, a weak absorption peak at  $277 \text{ cm}^{-1}$  is indicative of interlayer potassium vibrations typical of triclinic birnessite [35]. The possible presence of hexagonal birnessite is suggested by a weak band at  $570 \text{ cm}^{-1}$ , corresponding to the  $E_{2g}$  ( $\nu_{1\nu_1}$ ) mode associated with Mn–O–Mn symmetric stretching vibrations in the basal plane of the  $[MnO_6]$  groups, characteristic of hexagonal birnessite [36]. This peak is more prominent in materials synthesized by Mn(VI or VII) reduction with ethanol (M4 and M5), while it is barely detectable in the M2 oxide, consistent with the similarity in the synthetic route between M1 and M2, see Fig. S6 in SI section. On the other hand, the Raman spectra of M3, and to some extent also the M4 one, reflect the

low crystallinity of both materials, appearing as broad, single bands. The FTIR spectrum of M1 electrode reported in Fig. S7 SI section, features a broad band from  $3500\text{ cm}^{-1}$  to  $2500\text{ cm}^{-1}$ , corresponding to the symmetric and asymmetric stretching of O—H groups in interlayer structural water. Peaks at  $1636\text{ cm}^{-1}$  and  $1509\text{ cm}^{-1}$  are associated with O—H stretching from surface-adsorbed water, while bands at  $1056\text{ cm}^{-1}$  and  $926\text{ cm}^{-1}$  represent the complex vibrations involving -OH groups and Mn atoms [35]. The small peaks at  $551\text{ cm}^{-1}$  indicate Mn-O-Mn stretching modes in the structural octahedral layers of birnessite, consistent with triclinic birnessite [37,38]. In the M2 FTIR spectrum, a peak at  $2969\text{ cm}^{-1}$  attributed to the PVDF binder signifies the presence of CH<sub>2</sub> groups belonging to the polymer binder [39]. Fig. 2c reports the X-ray photoelectron spectroscopy (XPS) spectra for the Mn2p<sub>3/2</sub>, Mn3p, and Mn3s core levels, revealing the presence of Mn in multiple oxidation states (i.e. Mn(IV), Mn(III), and Mn(II)). The peaks were fitted according to the method reported by Ilton et al., with adjustments to peak widths based on instrumental resolution [40]. The survey spectrum and a table listing all fitting parameters are reported in Fig. S8 and Table S2 in SI section. The average oxidation state (AOS) derived from the three fitted core levels showed 56 % Mn(IV), 37 % Mn(III), and 7 % Mn(II), closely matching the values reported by Ilton et al. for triclinic birnessite. The calculated average oxidation number was 3.49, in good agreement with the results obtained from the oxalic acid back-titration method. Interestingly, the AOS determined by XPS decreased to 3.25 in the conversion anode electrode, possibly due to partial oxidation of the NMP solvent used in slurry preparation, given the high reactivity of M1. Additionally, no impurities brought about by the mining tailings or the synthesis process were detected on the M1 surface. The C1s peak showed three different carbon species, all originating from the carbon tape, while the K2p core level displayed a single pair of peaks, consistent with triclinic birnessite. Fig. 2d shows the nitrogen adsorption-desorption isotherms and the associated pore size distribution for M1. The adsorption-desorption curves suggest that the material is primarily composed of non-porous or macroporous aggregates, as can be inferred by the type II isotherm according to IUPAC classification. Such findings are consistent with and supported by SEM images. Therefore, macropores and interparticle pores largely account for material porosity. However, a small hysteresis loop resembling a type IV isotherm typical of mesoporous materials can also be identified. The specific surface area (SSA) determined by BET analysis was  $38 \pm 1\text{ m}^2/\text{g}$ , consistent with the values observed for poorly crystalline oxides used in alkaline batteries. For comparison, the SSA of electrolytic manganese oxide, commonly used in portable primary batteries, typically ranges between 10 and  $60\text{ m}^2/\text{g}$  [41]. Birnessites synthesized using deep eutectic solvents (DESs) have also shown BET SSA values close to that of M1 [29]. The average macropore diameter of 70 nm, derived from the N<sub>2</sub> adsorption/desorption curves, aligns with SEM micrographs. Despite M1 being predominantly macroporous, micropores were also discovered from TEM images. The micropore surface area was  $7.7\text{ m}^2/\text{g}$ , accounting for about 20 % of the total SSA, with a Langmuir SSA of approximately  $54\text{ m}^2/\text{g}$ . Furthermore, the total pore volume was  $0.129\text{ cm}^3/\text{g}$ , and an additional peak at 1.7 nm in the pore size distribution suggests the presence of micropores.

### 2.3. Electrochemical performance of MnO<sub>x</sub> in lithium-half cell

The M1 sample obtained through the direct manganate reduction with H<sub>2</sub>O<sub>2</sub> in a highly alkaline environment, is a nanocrystalline, hydrated oxide with mixed-valency manganese (II, III, and IV). Its properties are comparable to those of commercial Permanox δ-MnO<sub>2</sub>, a byproduct of the O-toluenesulfonamide to saccharin conversion, which was used as cathode material in dry-cell batteries up until the late 1990s [42]. Unlike the preparation of Permanox, the synthesis of M1 does not require either acid washing or MnSO<sub>4</sub>/KMnO<sub>4</sub> treatments to produce a battery-active material. In addition, the purification steps typically employed in industrial processes to remove metals more noble than zinc, such as raising the pH and cementation, are unnecessary in this case.

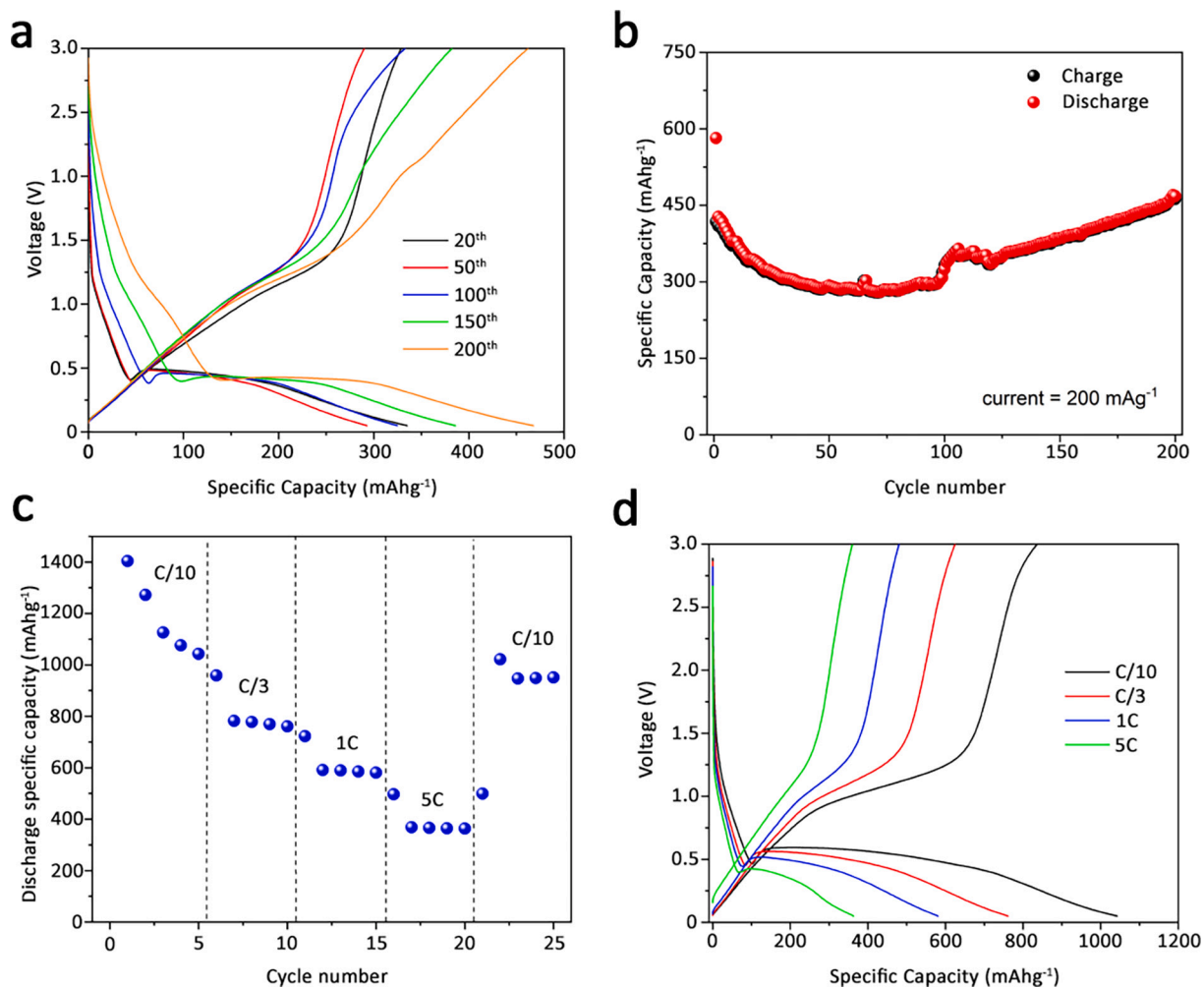
Moreover, preparing δ-MnO<sub>2</sub> directly from K<sub>2</sub>MnO<sub>4</sub>, using “green” and cost-effective reductants like hydrogen peroxide, sugars and bioethanol, could be more economically viable than synthesizing manganese oxides from commercially available permanganate. This cost advantage is due to the avoidance of the expensive Mn(VI) to Mn(VII) electrolytic oxidation process. Finally, the alkaline solution left over from M1 precipitation is amenable to reuse. These features make M1 a promising candidate as an active material for lithium metal batteries. Hence, M1 was evaluated as a material for conversion anode electrodes in lithium half-cells. Fig. 3 presents the electrochemical performance at a current density of 1C (200 mA/g, based on the MnO<sub>2</sub> mass), while additional testing at C/3 for M1 and the other MnO<sub>x</sub> materials (M2-M5) is shown in Fig. S9 SI section.

Fig. 3a illustrates the voltage profiles over different cycles and indicates a gradual decline in specific capacity during the initial cycles, followed by stabilization. Furthermore, the voltage profile highlights a multi-electron mechanism both during discharge and charge, as the evidence of 2 different plateaus both at discharge and charge. It is to be considered that the decrease and following increase in the delivered capacity is a common feature in conversion anodes and may stem from multiple sources. In particular, capacity fading is due to metallic particle size increase (i.e. lithium storage slower kinetics) and to a polymeric gel-like film, deriving from electrolyte decomposition, which grows on the surface of the crumbling anode. Furthermore, conversion anode operation results in the formation of new phases characterized by the uncontrolled spatial distribution originated from chemical interaction with large amounts of Li. Thus, insulating compounds with low conductivity are generated, leading to high overpotentials, degradation of the electrode and reduced reversible capacity. On the other hand, the increase of delivered capacity is due to the electronic conduction activation of Mn-particles upon lithium storage [43–45]. By the 100th cycle, the specific capacity stabilizes at about 300 mAh/g, indicating good cycling stability, as corroborated by the extended cycling data in Fig. 3b. The rate capability results reported in Fig. 3c demonstrate that the M1 electrode maintains a high specific capacity across a wide range of current rates, from C/10 to 5C. Even at 5C, the electrode delivers a significant capacity, above 300 mAh/g, suggesting that the material performs efficiently under high-rate conditions. Furthermore, when the current rate is reduced back to C/10, the electrode recovers 90 % of the specific capacity at cycle 5th, indicating the robust structural integrity and reversibility of the electrode during rapid cycling. Finally, specific capacity is around 800–900 mAh/g at C/3 (67 mA/g) over a 100 cycles range, see Fig. S9 in the SI section. These findings suggest that M1 exhibits excellent electrochemical properties, including both long-term cycling stability at 1C and impressive rate capability. The ability to sustain capacity at higher current rates, along with the capacity recovery when returning to lower rates, underscores M1’s potential as a promising material for high-power lithium-ion battery applications.

Cyclic Voltammetry (CV) curves for the first five cycles of M1 in a lithium half-cell is reported in Fig. S10 SI section. During the first cycle, a cathodic peak at 0.6 V is observed. This peak is associated to the electrolyte reduction and to the formation of solid electrolyte interface (SEI), which is absent in the subsequent cycles. Following SEI formation, a major cathodic peak at 0.3 V is observed, assigned to the reduction of δ-MnO<sub>2</sub> to lower oxidation states and, eventually, to metallic Mn, accompanied by Li<sub>2</sub>O formation [46]. Considering the oxidation process, only one peak occurring at around 1.1 V was detected. After the first cycle, characterized by a low Coulombic efficiency and a initial reduction in the CV curve area, the electrochemical process stabilizes, see Fig. S10 and S11 in the SI section.

### 2.4. Insight electrochemical mechanism of MnO<sub>x</sub> in lithium-half cell

In order to better understand the electrochemical conversion mechanisms, an ex-situ XRD study was conducted at different charge and discharge stages to correlate the voltage profile with structural



**Fig. 3.** M1 electrochemical performances. Cycling performance of an M1 electrode in Li-half-cell at a current of 200 mA/g. **(a)** Voltage profiles at different cycles and **(b)** prolonged cycling performance. **(c)** Rate capability analysis at different current rate and corresponding voltage profile; cell configuration Li/EC:DMC 1:1 LiPF<sub>6</sub> 1.0 M /MnO<sub>x</sub>.

changes. Fig. 4a reports the voltage profile at C/10 rate, displaying distinct plateaus which indicates the sequential reduction and oxidation of manganese as lithium ions intercalate and de-intercalate in/from the M1 structure. Conversely, the prominent plateau around 0.4 V during

discharge signifies the reduction of Mn to lower oxidation states, while the charging profile confirms the largely reversible nature of the redox reaction. These characteristics imply that M1 can facilitate multi-electron processes, thus enabling significant lithium storage to occur.

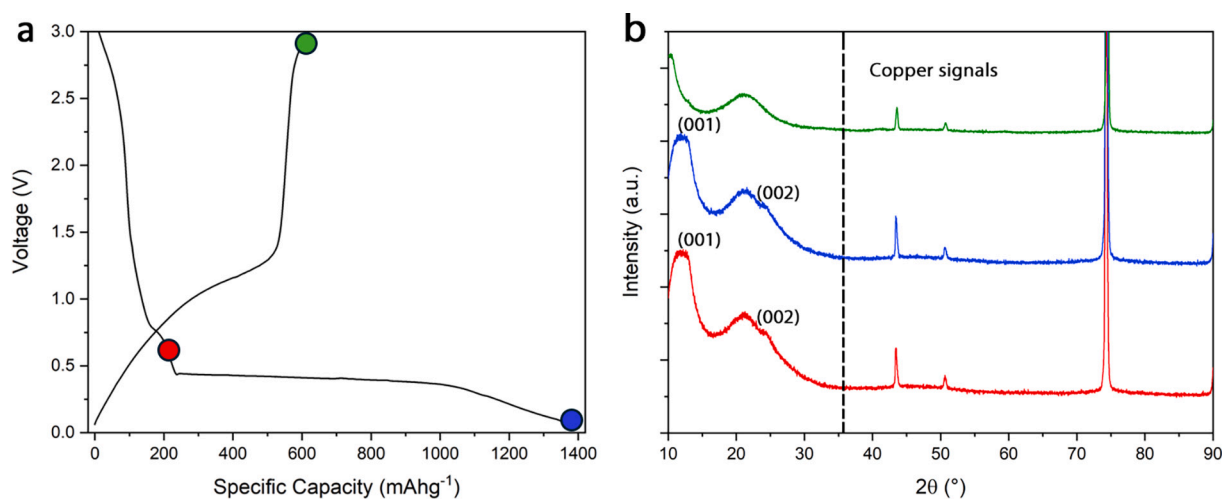


**Fig. 4.** Investigation of electrochemical mechanisms in Li-cell. **(a)** First cycle voltage profile at C/10 current rate of Li/M1 cell and **(b)** corresponding diffraction analysis at different states of discharge/charge.

Fig. 4b shows X-ray diffraction patterns at various states of charge and discharge, revealing structural evolution during cycling. Notably, during both partial and full discharge, the birnessite basal plane peak (001) is still visible, although broadened, indicating that the first discharge does not completely degrade the structure. Additionally, the (002) plane is detectable as a shoulder of the large super P carbon peak centered around  $21^\circ$  [47]. Upon full charging, the XRD pattern suggests that the M1 structure becomes nearly amorphous, as the (001) and (002) peaks weaken significantly. This loss of crystallinity may explain the decline in M1 specific capacity during the initial cycles. Nevertheless, amorphous materials can accommodate substantial volume changes associated with lithium ion insertion, allowing for rapid charge transfer. The capacity recovery observed after several cycles suggests that M1 structural changes are reversible. This property is crucial for the electrochemical performance in order to retain long-term cycling stability. Such a reversible behavior implies that M1 can undergo phase transformations without significant degradation of its electrochemical properties. Overall, Fig. 4 demonstrates that M1 not only shows clear voltage plateaus indicative of redox activity but also undergoes reversible structural transitions, which are essential for its performance as a lithium-ion battery electrode material.

Several factors contribute to M1's remarkable performances as conversion anode material. The layered structure, characterized by a certain degree of structural order and the presence of interlamellar water, likely provides effective ionic pathways for  $\text{Li}^+$  diffusion, enhancing the material's specific capacity [48–50]. Additionally, the closely spaced nanosheets of M1 facilitate fast charge transfer due to the increased contact area and to the reduced electron transport distance [51–54]. Furthermore, it has been widely reported that nanocrystalline manganese oxides shorten  $\text{Li}^+$  diffusion length and promote interfacial charge transfer [55,56]. The relatively low average oxidation state of manganese ( $\approx 3.50$ ) implies a high density of defects and active sites on M1 surface, which enhances the electrochemical reactivity. Furthermore, the open, sponge-like hierarchical morphology of M1 can accommodate the volume changes associated with  $\text{Li}^+$  insertion, preventing structural collapse and maintaining electrode integrity [57–60]. Interlayer water may also play a role in the electrochemical process by interacting with  $\text{Li}^+$  ions because of the high hydration enthalpy of lithium, potentially enhancing ionic mobility within the material [61,62]. Moreover, M1's combination of large macropores and some micropores favors efficient electrolyte contact with the active material, which is fundamental for rapid ion exchange. In contrast, the similarly synthesized M2 oxide suffers from a lack of long-range order, which may hinder both electron and ion transport. Even less crystalline materials like M3, M4, and M5 performed poorly as conversion anodes due to their disordered structures. Additionally, M1's higher purity compared to M3, M4, and M5 probably pre-empt parasitic reactions, thereby maximizing the specific capacity and enhancing the overall electrochemical performance.

### 3. Conclusion

This study presents a sustainable method for synthesizing  $\delta\text{-MnO}_2$  from manganese ore tailings sourced from the Brazilian Amazon, demonstrating its potential as anode material for lithium-ion batteries (LiBs). The process achieved a high manganese extraction rate (90.3 %) using oxidative alkaline fusion, aligning with circular economy principles. Through direct reduction of potassium manganate with  $\text{H}_2\text{O}_2$ , we obtained a K-birnessite-like material with mixed valency ( $\text{Mn}^{3+}/\text{Mn}^{4+}$ ), allowing for the recovery and reuse of the KOH solution. The resulting material (M1:  $\text{K}_{0.27}\text{MnO}_2 \cdot 0.6\text{H}_2\text{O}$ ) is a nanocrystalline, macroporous  $\delta\text{-MnO}_2$  with some structural order, which supports lithium storage through reversible redox reactions. The  $\text{H}_2\text{O}_2$ -based synthesis produced a pure material, free from impurities, despite the original manganese source. M1 showed promising electrochemical performance, with stable cycling at 1C (200 mA/g) and a capacity of 300–400 mAh/g, reaching

800–900 mAh/g at C/3 (67 mA/g), and strong rate capability across various current densities. Electrochemical analysis revealed reversible phase transformations during cycling, essential for long-term stability and comparable with hydrothermal synthesis starting from commercial reagents, see Table S4 in SI section. Key features such as hierarchical morphology, interlayer water, layered nanostructure, and high purity contributed to M1 superior performance compared to other  $\text{MnO}_x$  materials derived from the same tailings (M2–M5). Overall, M1 combines high Mn recovery, sustainable synthesis, and robust electrochemical properties, making it a strong candidate for high-power, eco-friendly LiBs. This approach offers a pathway for valorizing manganese mining residues, addressing the demand for critical battery materials in a resource-efficient manner.

## 4. Experimental

### 4.1. Materials

Potassium hydroxide (KOH flakes, >85 % purity), oxalic acid (99 %), sulfuric acid (98 %), hydrogen peroxide (30 % solution), NMP (N-Methyl-2-pyrrolidone), and PVDF (polyvinylidene difluoride) were obtained from Sigma-Aldrich. Potassium permanganate ( $\text{KMnO}_4$ ) was supplied by Carlo Erba (Italy), hydrochloric acid (HCl, 37 %) by Vetec (Brazil), and absolute ethanol by EMSURE. All chemicals were used as received. Super P carbon was acquired from Timcal (Singapore), and LP30 electrolyte from BASF. Manganese ore tailings used in the study were sourced from the VALE S.A. Azul mining site in the Carajas mining district, Pará, Brazil, collected from the decommissioned Kalunga dam.

### 4.2. Manganese extraction as $\text{K}_2\text{MnO}_4$

For manganese recovery, 10 g of tailings, milled for 2 h to increase surface area, were used. The recovery process, based on Da Rocha et al. for battery recycling [63], involved adding a 6 M KOH solution to the sample in a nickel crucible (KOH-to-tailings ratio: 2:1). After drying at  $120^\circ\text{C}$ , the mixture underwent oxidative alkaline fusion at  $350^\circ\text{C}$  for 1 h. The process was repeated twice by adding 10 mL of distilled water (at  $150^\circ\text{C}$ ) at each stage.  $\text{K}_2\text{MnO}_4$  was leached with a 1.7 M KOH solution through sonication and stirring. The amount of extracted Mn was evaluated by disproportioning the  $\text{K}_2\text{MnO}_4$  solution to  $\text{MnO}_2$  and  $\text{KMnO}_4$ . The latter concentration was determined spectrophotometrically and allowed for the amount of recovered  $\text{K}_2\text{MnO}_4$  and, therefore, the Mn extraction efficiency to be calculated.

### 4.3. $\text{MnO}_x$ synthesis

A 0.075 M  $\text{K}_2\text{MnO}_4$  solution, diluted from the recovered batch, was used to synthesize  $\text{MnO}_x$ . Briefly,  $\text{H}_2\text{O}_2$  (30 %, 21 mL) was added dropwise to 110 mL of the solution, stirred for 3 h, then washed and dried at  $110^\circ\text{C}$ , yielding the material labeled M1. The KOH-rich filtrate was recovered and stored for other applications. Other  $\text{MnO}_x$  materials (M2–M5) were synthesized from the same batch using varied methods (details in Supporting Information).

### 4.4. Materials characterization

The structural features of tailings and  $\text{MnO}_x$  materials were characterized using XRD (Rigaku Smart-Lab, Cu  $\text{K}\alpha$  radiation). Elemental composition of tailings was determined by ED-XRF (X-Lab 2000). M1 composition was analyzed using the oxalic acid-permanganate titration method for oxidation state determination and FAAS (with a PinAAcle 900 T spectrometer by PerkinElmer) for potassium and manganese quantification. TGA-DTA was performed to analyze thermal behavior. Raman spectra were collected at 632 nm laser excitation, using a Jobin Yvon labRam HR UV 800. BET surface area and pore size distribution were measured by nitrogen adsorption/desorption (ASAP 2020 V3). XPS

was conducted with a JEOL JPS-9030 (equipped with a non-monochromated 300 W Al source) setup for surface composition analysis. The analyzer binding energy scale was calibrated by measuring sputter cleaned gold and copper foils and setting the Au<sub>4f<sub>7/2</sub></sub> peak to 84.00 eV and the Cu<sub>2p<sub>3/2</sub></sub> peak to 932.62 eV CasaXPS software was used for peak fitting [64]. The morphological analysis of the materials has been performed using a FESEM Zeiss Auriga, equipped with Bruker Quantax EDX spectrometer and TEM JEOL F-200 assembled with a GATAN Rio16 CMOS acquisition camera and a JEOL EDX spectrometer, while XPS was conducted with a JEOL JPS-9030 setup for surface composition analysis.

#### 4.5. Electrode preparation and electrochemical testing

MnO<sub>x</sub> electrodes were prepared by mixing MnO<sub>x</sub> (70 wt%), PVDF (10 wt%), and Super P carbon (20 wt%) in NMP, then casting on copper foil and drying at 100 °C. Coin cells were assembled with LP30 electrolyte, and electrochemical testing was performed using a Maccor battery tester, cycling between 0.01 and 3.0 V. Current of 200 mA/g was referred in the text as 1C, however not being referred to current to discharge the material in 1 h.

#### CRedit authorship contribution statement

**L. Angeletti:** Investigation. **M. Agostini:** Writing – review & editing, Methodology, Data curation, Conceptualization. **B.A. Miranda Figueira:** Resources, Investigation, Formal analysis, Data curation. **A. Latini:** Investigation, Conceptualization. **E.C. Paris:** Investigation. **F. De Giorgio:** Funding acquisition, Conceptualization. **T. Schultz:** Investigation, Formal analysis, Data curation. **C. Di Conzo:** Formal analysis. **F. Mura:** Formal analysis. **M. Rossi:** Funding acquisition, Formal analysis. **N.G. Yadav:** Formal analysis. **P. Adelhelm:** Formal analysis. **F. Mazzei:** Funding acquisition. **S. Brutti:** Validation, Supervision, Resources, Funding acquisition, Conceptualization. **S. Quaranta:** Writing – original draft, Methodology, Investigation, Data curation, Conceptualization.

#### Declaration of competing interest

None.

#### Acknowledgements

Authors would like to thank Prof. Marcondes da Silva (UFPA) and VALE S.A. for providing Amazon mining tailings. TEM investigation was carried out with the support of the «Advanced Tomography and Microscopy» (ATOM) project) granted by Lazio Region (protocol number #173-2017-17395 L.R: 13/200. XRD measurements performed at the ISMN-CNR SURFACE facility. F.D.G. and S.Q. acknowledge the following funding projects: PNRR MUR project ECS\_00000033\_ECO-SISTER; Mission Innovation Program MiSE under the Grant “Italian Energy Materials Acceleration Platform—IEMAP”; Prin 2022 “DiGreen: A digital and chemical approach for green recycling of Li-based batteries” (no. 2022W37L2L)—MUR (Ministero Italiano dell’Università e della Ricerca); ROMA’S – Recovery of Zn and Mn for sustainable electrochemical energy storage and conversion systems, FOE FutuRaw - “Riparto Fondo Ordinario Enti di Ricerca Ministero dell’Università e della Ricerca”. Finally, S.Q., F.D.G. and E.C.P. wish to thank the EMBRAPA-CNR (ISMN) Scientific Cooperation Project (CNR protocol number 2023-CNR0A00-0024560).

#### Appendix A. Supplementary data

Supplementary data to this article can be found online at <https://doi.org/10.1016/j.susmat.2025.e01347>.

#### Data availability

Data will be made available on request.

#### References

- [1] International Energy Agency, Net Zero by 2050: A Roadmap for the Global Energy Sector, 2021, p. 70.
- [2] J.B. Goodenough, K.S. Park, The Li-ion rechargeable battery: a perspective, *J. Am. Chem. Soc.* 135 (2013) 1167–1176, <https://doi.org/10.1021/ja3091438>.
- [3] A. Manthiram, A reflection on lithium-ion battery cathode chemistry, *Nat. Commun.* 11 (2020) 1–9, <https://doi.org/10.1038/s41467-020-15355-0>.
- [4] J. Asenbauer, T. Eisenmann, M. Kuenzel, A. Kazzazi, Z. Chen, D. Bresser, The success story of graphite as a lithium-ion anode material-fundamentals, remaining challenges, and recent developments including silicon (oxide) composites, *sustain, Energy Fuel* 4 (2020) 5387–5416, <https://doi.org/10.1039/d0se00175a>.
- [5] J. Yue, X. Gu, L. Chen, N. Wang, X. Jiang, H. Xu, J. Yang, Y. Qian, General synthesis of hollow MnO<sub>2</sub>, Mn<sub>3</sub>O<sub>4</sub> and MnO nanospheres as superior anode materials for lithium ion batteries, *J. Mater. Chem. A* 2 (2014) 17421–17426, <https://doi.org/10.1039/c4ta03924f>.
- [6] S.P. Poizot, S. Laruelle, S. Grugeon, L. Dupont, J.-M. Tarasco, Nano-sized transition-metaloxides-as-negative-electrode materials for lithium-ion batteries, *Nature* 407 (2000) 496.
- [7] Y. Guo, D. Zhang, Z. Bai, Y. Yang, Y. Wang, J. Cheng, P.K. Chu, Y. Luo, MXene nanofibers confining MnOx nanoparticles: a flexible anode for high-speed lithium ion storage networks, *Dalton Trans.* 51 (2022) 1423–1433, <https://doi.org/10.1039/d1dt03718h>.
- [8] S. Sun, J. Li, C. Xu, T. Zhai, H. Xia, Manganese-based layered oxides for electrochemical energy storage: a review of degradation mechanisms and engineering strategies at the atomic level, *J. Mater. Chem. A* 10 (2022) 19231–19253, <https://doi.org/10.1039/d2ta02242g>.
- [9] J.A. Llamas-Orozco, F. Meng, G.S. Walker, A.F.N. Abdul-Manan, H.L. MacLean, I. D. Posen, J. McKechnie, Estimating the environmental impacts of global lithium-ion battery supply chain: a temporal, geographical, and technological perspective, *PNAS Nexus* 2 (2023) 1–16, <https://doi.org/10.1093/pnasnexus/pgad361>.
- [10] H.M. Queiroz, S.C. Ying, M. Abernathy, D. Barcellos, F.A. Gabriel, X.L. Otero, G. N. Nóbrega, A.F. Bernardino, T.O. Ferreira, Manganese: the overlooked contaminant in the world largest mine tailings dam collapse, *Environ. Int.* 146 (2021), <https://doi.org/10.1016/j.envint.2020.106284>.
- [11] European Commission, Framework for Ensuring a Secure and Sustainable Supply of Critical Raw Materials 2023, 2023, pp. 1–94, <https://doi.org/10.2760/386650>.
- [12] S. Mancini, M. Casale, A. Tazzini, G.A. Dino, Use and recovery of extractive waste and tailings for sustainable raw materials supply, *Mining* 4 (2024) 149–167, <https://doi.org/10.3390/mining4010010>.
- [13] V.J. Ingram-Jones, R.C.T. Slade, T.W. Davies, J.C. Southern, S. Salvador, Dehydroxylation sequences of gibbsite and boehmite: study of differences between soak and flash calcination and of particle-size effects, *J. Mater. Chem.* 6 (1996) 73–79, <https://doi.org/10.1039/jm9960600073>.
- [14] B.A.M. Figueira, R.S. Angélica, M.L. da Costa, H. Pöllmann, K. Schenzel, Conversion of different Brazilian manganese ores and residues into birnessite-like phyllosulfate, *Appl. Clay Sci.* 86 (2013) 54–58, <https://doi.org/10.1016/j.clay.2013.10.016>.
- [15] B.A.M. Figueira, R.S. Angélica, M.L. Da Costa, D. Biggemann, J.M.R. Mercury, H. Pöllmann, Hydrothermal synthesis of Na-birnessite-type material using ores from Carajás (Amazon region, Brazil) as Mn source, *Microporous Mesoporous Mater.* 179 (2013) 212–216, <https://doi.org/10.1016/j.micromeso.2013.06.011>.
- [16] B. Liu, Y. Zhang, M. Lu, Z. Su, G. Li, T. Jiang, Extraction and separation of manganese and iron from ferruginous manganese ores: a review, *Miner. Eng.* 131 (2019) 286–303, <https://doi.org/10.1016/j.mineng.2018.11.016>.
- [17] P. Li, S. Hua, X. Wang Luo, L. Wang, J. Wang, F. Teng, Q. Wang, Y. Zhang, X. Liu, H. Zhang, J. Liang, X. Duan, Study on the high-efficiency separation of Fe and Mn from low-grade pyrolusite and the preparation of LiMn<sub>2</sub>O<sub>4</sub> materials for lithium-ion batteries, *Sep. Purif. Technol.* 278 (2022) 119611, <https://doi.org/10.1016/j.seppur.2021.119611>.
- [18] S. Ching, D.J. Petrovay, M.L. Jorgensen, S.L. Suib, Sol-gel synthesis of layered Birnessite-type manganese oxides, *Inorg. Chem.* 36 (1997) 883–890, <https://doi.org/10.1021/ic961088d>.
- [19] Y. Ma, J. Luo, S.L. Suib, Syntheses of birnessites using alcohols as reducing reagents: effects of synthesis parameters on the formation of birnessites, *Chem. Mater.* 11 (1999) 1972–1979, <https://doi.org/10.1021/cm980399e>.
- [20] Q. Feng, H. Kanoh, K. Ooi, Manganese oxide porous crystals, *J. Mater. Chem.* 9 (1999) 319–333, <https://doi.org/10.1039/a805369c>.
- [21] L.D. Kulish, P. Nukala, R. Scholtens, A.G.M. Uiterwijk, R. Hamming-Green, G. R. Blake, Structural modulation in potassium birnessite single crystals, *J. Mater. Chem. C* 9 (2021) 1370–1377, <https://doi.org/10.1039/d0tc05396a>.
- [22] Y. Li, G. Jiang, N. Ouyang, Z. Qin, S. Lan, Q. Zhang, The controlled synthesis of birnessite nanoflowers via H<sub>2</sub>O<sub>2</sub> reducing KMnO<sub>4</sub> for efficient adsorption and photooxidation activity, *Front. Chem.* 9 (2021) 1–8, <https://doi.org/10.3389/fchem.2021.699513>.
- [23] L. Liu, Y. Luo, W. Tan, Y. Zhang, F. Liu, G. Qiu, Facile synthesis of birnessite-type manganese oxide nanoparticles as supercapacitor electrode materials, *J. Colloid Interface Sci.* 482 (2016) 183–192, <https://doi.org/10.1016/j.jcis.2016.07.077>.

- [24] C. Jiang, Z. Tang, Z. Zhang, Facile synthesis of a hierarchical manganese oxide hydrate for superior lithium-ion battery anode, *Ionics* (Kiel) 25 (2019) 3577–3586, <https://doi.org/10.1007/s11581-019-02909-6>.
- [25] C. Liu, Y. Chen, W. Huang, Y. Situ, H. Huang, Birnessite manganese oxide nanosheets assembled on Ni foam as high-performance pseudocapacitor electrodes: electrochemical oxidation driven porous honeycomb architecture formation, *Appl. Surf. Sci.* 458 (2018) 10–17, <https://doi.org/10.1016/j.apsusc.2018.06.243>.
- [26] A.C. Alves, J.P. Correia, T.M. Silva, M.F. Montemor, Electrochemical insights into the energy storage mechanism of birnessite in aqueous solutions, *Electrochim. Acta* 454 (2023) 142418, <https://doi.org/10.1016/j.electacta.2023.142418>.
- [27] W. Yang, Y. Zhu, F. You, L. Yan, Y. Ma, C. Lu, P. Gao, Q. Hao, W. Li, Insights into the surface-defect dependence of molecular oxygen activation over birnessite-type MnO<sub>2</sub>, *Appl. Catal. B Environ.* 233 (2018) 184–193, <https://doi.org/10.1016/j.apcatb.2018.03.107>.
- [28] G. Zhu, L. Deng, J. Wang, L. Kang, Z.H. Liu, The simple preparation of birnessite-type manganese oxide with flower-like microsphere morphology and its remarkable capacity retention, *Mater. Res. Bull.* 47 (2012) 3533–3537, <https://doi.org/10.1016/j.materresbull.2012.06.065>.
- [29] L. Ding, Z. Li, L. Chen, Z. Qi, Ultrafast synthesis of K cations inserted birnessite-type MnO<sub>2</sub> electrode in ethanolamine based deep eutectic solvents with improved supercapacitor performance, *Electrochim. Acta* 455 (2023) 142424, <https://doi.org/10.1016/j.electacta.2023.142424>.
- [30] Y. Zeng, X. Yang, H. Yu, Birnessite MnO<sub>2</sub> supported on CNTs in-situ for low-temperature oxidation of ethyl acetate, *Carbon Res.* 1 (2022) 1–15, <https://doi.org/10.1007/s44246-022-00024-2>.
- [31] D.C. Golden, J.B. Dixon, C.C. Chen, Ion exchange, thermal transformations, and oxidizing properties of birnessite, *Clay Clay Miner.* 34 (1986) 511–520, <https://doi.org/10.1346/CCMN.1986.0340503>.
- [32] S. Zhu, W. Huo, X. Liu, Y. Zhang, Birnessite based nanostructures for supercapacitors: challenges, strategies and prospects, *Nanoscale Adv.* 2 (2020) 37–54, <https://doi.org/10.1039/c9na00547a>.
- [33] B.R. Bolton, R. Both, N.F. Exon, T.F. Hamilton, J. Ostwald, J.D. Smith, Geochemistry and mineralogy of seafloor hydrothermal and hydrogenetic Mn oxide deposits from the Manus Basin and Bismarck archipelago region of the Southwest Pacific Ocean, *Mar. Geol.* 85 (1988) 65–87, [https://doi.org/10.1016/0025-3227\(88\)90084-9](https://doi.org/10.1016/0025-3227(88)90084-9).
- [34] M.V. Ananth, K. Dakshinamurthi, Electrolytic manganese dioxides for battery applications: studies using electron paramagnetic resonance, *J. Power Sources* 40 (1992) 355–360, [https://doi.org/10.1016/0378-7753\(92\)80024-6](https://doi.org/10.1016/0378-7753(92)80024-6).
- [35] J. Preudhomme, P. Tarte, Infrared studies of spinels-II. The experimental bases for solving the assignment problem, *Spectrochim. Acta Part A Mol. Spectrosc.* 27 (1971) 845–851, [https://doi.org/10.1016/0584-8539\(71\)80163-0](https://doi.org/10.1016/0584-8539(71)80163-0).
- [36] K.C. Mendes, B.A.M. Figueira, T.C.C. Lavra, O.J.C. Fernandez, P.C. Gómez, J. M. Rivas Mercury, Hydrothermal synthesis of o-LiMnO<sub>2</sub> employing Mn mining residues from Amazon (Brazil) as starting material, *Mater. Lett. X* 2 (2019) 100012, <https://doi.org/10.1016/j.mblux.2019.100012>.
- [37] A. Chemistry, Syntheses and Characterization of 21, 1983, pp. 31–39.
- [38] M. Liang, H. Guo, W. Xiu, Arsenite Oxidation and Arsenic Adsorption on Birnessite in the Absence and the Presence of Citrate or EDTA, 2020, pp. 43769–43785.
- [39] K.A.R. Medeiros, E.Q. Rangel, A.R. Sant'Anna, D.R. Louzada, C.R.H. Barbosa, J.R. M. D'Almeida, Evaluation of the electromechanical behavior of polyvinylidene fluoride used as a component of risers in the offshore oil industry, *Oil Gas Sci. Technol.* 73 (2018), <https://doi.org/10.2516/ogst/2018058>.
- [40] E.S. Ilton, J.E. Post, P.J. Heaney, F.T. Ling, S.N. Kerisit, XPS determination of Mn oxidation states in Mn (hydr)oxides, *Appl. Surf. Sci.* 366 (2016) 475–485, <https://doi.org/10.1016/j.apsusc.2015.12.159>.
- [41] E.S. Treatments, C. Hardening, A. Alloys, A. Compounds, MANGANESE AND 7, 2024.
- [42] K.J. Euler, H. Mueller-Helsa, Electrical characteristics of a highly hydrated battery grade manganese dioxide powder, *J. Power Sources* 4 (1979) 77–89, [https://doi.org/10.1016/0378-7753\(79\)80039-7](https://doi.org/10.1016/0378-7753(79)80039-7).
- [43] D. Puthusseri, M. Wahid, S. Ogale, Conversion-type anode materials for alkali-ion batteries: state of the art and possible research directions, *ACS Omega* 3 (2018) 4591–4601, <https://doi.org/10.1021/acsomega.8b00188>.
- [44] C.K. Chan, R.N. Patel, M.J. O'Connell, B.A. Korgel, Y. Cui, Solution-grown silicon nanowires for lithium-ion battery anodes, *ACS Nano* 4 (2010) 1443–1450, <https://doi.org/10.1021/nn901409q>.
- [45] D. Narsimulu, S. Ghosh, M. Bhar, S.K. Marthia, Electrochemical studies on kinetics and diffusion of Li-ions in MnO<sub>2</sub> electrodes, *J. Electrochem. Soc.* 166 (2019) A2629–A2635, <https://doi.org/10.1149/2.1161912jes>.
- [46] Y.C. Tsai, C.T. Kuo, S.F. Liu, Y.T. Lee, T.R. Yew, Effect of different electrolytes on MnO<sub>2</sub> Anodes in Lithium-ion batteries, *J. Phys. Chem. C* 125 (2021) 1221–1233, <https://doi.org/10.1021/acs.jpcc.0c09022>.
- [47] J. Mok, D. Choi, S.H. Bhang, Environmentally friendly route for fabricating conductive agent for lithium-ion batteries: carbon nanoparticles derived from polyethylene, *Catalysts* 11 (2021), <https://doi.org/10.3390/catal11040424>.
- [48] L. Cong, H. Xie, J. Li, Hierarchical structures based on two-dimensional nanomaterials for rechargeable Lithium batteries, *Adv. Energy Mater.* 7 (2017), <https://doi.org/10.1002/aenm.201601906>.
- [49] Y. Wang, H. Li, P. He, E. Hosono, H. Zhou, Nano active materials for lithium-ion batteries, *Nanoscale* 2 (2010) 1294–1305, <https://doi.org/10.1039/c0nr00068j>.
- [50] C. Jiang, Y. Li, S. Wang, Z. Zhang, Z. Tang, Hierarchical hydrated WO<sub>3</sub>·0.33H<sub>2</sub>O/graphene composites with improved lithium storage, *Electrochim. Acta* 278 (2018) 290–301, <https://doi.org/10.1016/j.electacta.2018.04.169>.
- [51] S.Z. Huang, Q. Zhang, W. Yu, X.Y. Yang, C. Wang, Y. Li, B.L. Su, Grain boundaries enriched hierarchically mesoporous MnO<sub>2</sub>/carbon microspheres for superior Lithium ion battery anode, *Electrochim. Acta* 222 (2016) 561–569, <https://doi.org/10.1016/j.electacta.2016.11.009>.
- [52] Y. Sun, X. Hu, W. Luo, F. Xia, Y. Huang, Reconstruction of conformal nanoscale MnO on graphene as a high-capacity and long-life anode material for lithium ion batteries, *Adv. Funct. Mater.* 23 (2013) 2436–2444, <https://doi.org/10.1002/adfm.201202623>.
- [53] Y.C. Zhang, J.T. Li, Z.G. Wu, L. Huang, S.G. Sun, Synthesis of hierarchical spindle-like Mn<sub>2</sub>O<sub>3</sub> for lithium ion batteries with enhanced lithium storage properties, *J. Alloys Compd.* 721 (2017) 229–235, <https://doi.org/10.1016/j.jallcom.2017.05.305>.
- [54] K.W. Nam, S. Kim, E. Yang, Y. Jung, E. Levi, D. Aurbach, J.W. Choi, Critical role of crystal water for a layered cathode material in sodium ion batteries, *Chem. Mater.* 27 (2015) 3721–3725, <https://doi.org/10.1021/acs.chemmater.5b00869>.
- [55] P. Liu, S.H. Lee, Y. Yan, C. Edwin Tracy, J.A. Turner, Nanostructured manganese oxides as lithium battery cathode materials, *J. Power Sources* 158 (2006) 659–662, <https://doi.org/10.1016/j.jpowsour.2005.10.005>.
- [56] S.M. Oh, I.Y. Kim, K. Adpakpang, S.J. Hwang, The beneficial effect of nanocrystalline and amorphous nature on the anode performance of manganese oxide for lithium ion batteries, *Electrochim. Acta* 174 (2015) 391–399, <https://doi.org/10.1016/j.electacta.2015.06.014>.
- [57] J. Choi, W.J. Byun, D. Kang, J.K. Lee, Porous manganese oxide networks as high-capacity and high-rate anodes for lithium-ion batteries, *Energies* 14 (2021), <https://doi.org/10.3390/en14051299>.
- [58] N.F.M. Yusoff, N.H. Idris, M.F.M. Din, S.R. Majid, N.A. Harun, M.M. Rahman, Investigation on the electrochemical performances of Mn<sub>2</sub>O<sub>3</sub> as a potential anode for Na-ion batteries, *Sci. Rep.* 10 (2020) 1–10, <https://doi.org/10.1038/s41598-020-66148-w>.
- [59] Y. Jiang, J.L. Yue, Q. Guo, Q. Xia, C. Zhou, T. Feng, J. Xu, H. Xia, Highly porous Mn<sub>3</sub>O<sub>4</sub> micro/nanocuboids with in situ coated carbon as advanced anode material for Lithium-ion batteries, *Small* 14 (2018) 1–9, <https://doi.org/10.1002/smll.201704296>.
- [60] H.S. Kim, D.W. Kim, S.S. Kim, C. Senthil, H.Y. Jung, Freestanding conversion-type anode via one-pot formation for flexible Li-ion battery, *Chem. Eng. J.* 427 (2022) 130937, <https://doi.org/10.1016/j.cej.2021.130937>.
- [61] H.J. Lee, J. Shin, J.W. Choi, Intercalated water and organic molecules for electrode materials of rechargeable batteries, *Adv. Mater.* 30 (2018) 1–14, <https://doi.org/10.1002/adma.201705851>.
- [62] N. Nitta, F. Wu, J.T. Lee, G. Yushin, Li-ion battery materials: present and future, *Mater. Today* 18 (2015) 252–264, <https://doi.org/10.1016/j.mattod.2014.10.040>.
- [63] R.A. Da Rocha, C.L. Quintanilha, T.V. Lanxin, J.C. Afonso, C.A. Vianna, V. Gante, J. L. Mantovano, Production of potassium manganate and barium manganate from spent zinc-MnO<sub>2</sub> dry cells via fusion with potassium hydroxide, *J. Power Sources* 268 (2014) 831–840, <https://doi.org/10.1016/j.jpowsour.2014.06.134>.
- [64] N. Fairley, V. Fernandez, M. Richard-Plouet, C. Guillot-Deudon, J. Walton, E. Smith, D. Flahaut, M. Greiner, M. Biesinger, S. Tougaard, D. Morgan, J. Baltrusaitis, Systematic and collaborative approach to problem solving using X-ray photoelectron spectroscopy, *Appl. Surf. Sci. Adv.* 5 (2021) 100112, <https://doi.org/10.1016/j.apsadv.2021.100112>.